A Prokaryotic Membrane Sculpting BAR Domain Protein

Daniel A. Phillips[1*], Lori A. Zacharoff[2*], Cheri M. Hampton[3], Grace W. Chong[4], Anthony P. Malanoski[5], Lauren Ann Metskas[6], Shuai Xu[2], Lina J. Bird[5], Brian J. Eddie[5], Grant J. Jensen[6,7], Lawrence F. Drummy[3], Mohamed Y. El-Naggar[2,4,8], and Sarah M. Glaven[5]

[1]American Society for Engineering Education, Washington, DC, USA.
[2]University of Southern California, Department of Physics and Astronomy, Los Angeles, CA 90089
[3]Materials and Manufacturing Directorate, Air Force Research Laboratory, Wright-Patterson Air Force Base, WPAFB, OH, USA.
[4]University of Southern California, Department of Biological Sciences, Los Angeles, CA 90089
[5]Center for Bio/Molecular Science and Engineering, Naval Research Laboratory, Washington, DC, USA.
[6]California Institute of Technology, Division of Biology and Biological Engineering, Pasadena, CA 91125
[7]California Institute of Technology, Howard Hughes Medical Institute, Pasadena, CA 91125
[8]University of Southern California, Department of Chemistry, Los Angeles, CA 90089

[*]These authors contributed equally to this work

Classification: Biological sciences

Keywords: BAR domain | extracellular electron transport | membrane shaping | outer membrane vesicles | outer membrane extensions | *Shewanella*

Send all correspondence to:
Daniel A. Phillips
Daniel.a.phillips62.ctr@mail.mil
(423) 215-2256
US Army CCDC CBC, Building E3549
Aberdeen Proving Grounds Edgewood Area
Gunpowder, MD 21010

Lori A. Zacharoff
zacharof@usc.edu
(763) 221-0960
920 Bloom Walk
SSC, 215C
Los Angeles, CA 90089

Abstract

Bin/Amphiphysin/RVS (BAR) domain proteins belong to a superfamily of coiled-coil proteins influencing membrane curvature in eukaryotes and are associated with vesicle biogenesis, vesicle-mediated protein trafficking, and intracellular signaling. Here we report the first prokaryotic BAR domain protein, BdpA, from *Shewanella oneidensis* MR-1, known to produce redox-active membrane vesicles and micrometer-scale outer membrane extensions (OMEs). BdpA is required for uniform size distribution of membrane vesicles and scaffolding OMEs into a consistent diameter and curvature. Cryogenic transmission electron microscopy reveals a strain lacking BdpA produces lobed, disordered OMEs rather than membrane tubes produced by the wild type strain. Overexpression of BdpA promotes OME formation during conditions where they are less common. Heterologous expression results in OME production in *Marinobacter atlanticus* and *Escherichia coli*. Based on the ability of BdpA to alter membrane curvature *in vivo*, we propose that BdpA and its homologs comprise a newly identified class of prokaryotic BAR (P-BAR) domains.

Introduction

Eukaryotic Bin/Amphiphysin/Rvs (BAR) domain-containing proteins generate membrane curvature through electrostatic interactions between positively charged amino acids and negatively charged lipids, scaffolding the membrane along the intrinsically curved surface of the antiparallel coiled-coil protein dimers (1-4). Some BAR domain-containing proteins, such as the N-BAR protein BIN1, contain amphipathic helical wedges that insert into the outer membrane leaflet and can assist in membrane binding (5). Other BAR domains can be accompanied by a membrane targeting domain, such as PX for phosphoinositide binding (6, 7), in order to direct membrane curvature formation at specific sites, as is the case with sorting nexin BAR proteins (8). The extent of accumulation of BAR domain proteins at a specific site can influence the degree of the resultant membrane curvature (9), and tubulation events arise as a consequence of BAR domain multimerization in conjunction with lipid binding (10). Interactions between BAR domain proteins and membranes resolve membrane tension, promote membrane stability, and aid in localizing cellular processes, such as actin binding, signaling through small GTPases, membrane vesicle scission, and vesicular transport of proteins (11-13). Despite our knowledge of numerous eukaryotic BAR proteins spanning a variety of modes of curvature formation, membrane localizations, and subtypes (N-BAR, F-BAR, and I-BAR), characterization of a functional prokaryotic BAR domain protein has yet to be reported.

Bacterial cell membrane curvature can be observed during the formation of outer membrane vesicles (OMV) and outer membrane extensions (OME). OMV formation is ubiquitous and has many documented functions (14). OMEs are less commonly

40 observed, remain attached to the cell, and various morphologies can be seen extending
41 from single cells including *Myxococcus xanthus* (15, 16), flavobacterium strain
42 Hel3_A1_48 (17), *Vibrio vulnificus* (18), *Francisella novicida* (19), *Shewanella oneidensis*
43 (20-23), and as cell-cell connections in *Bacillus subtilis* (24-26) and *Escherichia coli* (27).
44 Several bacterial proteins have demonstrated membrane tubule formation capabilities *in*
45 *vitro* (28-33), but despite the growing number of reports, proteins involved in shaping
46 bacterial membranes into OMV/Es have yet to be identified. Recently, researchers have
47 begun to suspect that OMV and OME formation has some pathway overlap (17), and it is
48 proposed that proteins are necessary to stabilize these structures (34).

49 *Shewanella oneidensis* is a model organism for extracellular electron transfer
50 (EET), a mode of respiration whereby electrons traverse the inner membrane, periplasm,
51 and outer membrane via multiheme cytochromes to reach exogenous insoluble terminal
52 electron acceptors, such as metals and electrodes (35, 36). *S. oneidensis* is known to
53 produce redox-active OMVs (37) and OMEs coated with mulitheme cytochromes,
54 particularly upon surface attachment (20, 22, 37). However, little is known about their
55 formation mechanism, control of shape or curvature, and electrochemical properties that
56 influence EET function.

57 Previously, OMEs of *S. oneidensis* were shown to transition between chains of
58 vesicles and tubules. We identified a component critical to this structural transition as the
59 first BAR domain protein in prokaryotes, which we term BdpA (BAR domain-like protein
60 A). Through comparative proteomics, cryogenic electron microscopy, and molecular
61 biology, we show that BdpA is enriched in OME/Vs, regulates size of OMVs, and controls
62 the shape of OMEs. Likewise, BdpA confers OME formation capabilities when expressed

63 in other bacteria, showing mechanistic evidence of BAR domain protein-mediated tubule
64 formation *in vivo*. This study provides a framework for prokaryotic BAR domain
65 characterization, and putative BAR domain-containing BdpA homologs in other bacteria
66 suggest BAR domain protein-mediated membrane sculpting is an evolutionarily
67 conserved function.

68 **Results and Discussion**

69 ***S. oneidensis* OMVs are redox-active and enriched with BdpA**

70 OMVs were purified from *S. oneidensis* cells grown in batch cultures to
71 characterize their redox features and unique proteome, as well as to identify putative
72 membrane shaping proteins. Cryogenic transmission electron microscopy (cryo-TEM)
73 tomographic reconstruction slices of the purified samples showed uniform OMVs with the
74 characteristic single membrane phenotype and an approximate diameter of 200 nm (Fig.
75 1a). Previous measurements showed OMVs can reduce extracellular electron
76 acceptors (37) and that vesicles from *G. sulfurreducens* can mediate electron transfer
77 (38). Electrochemical activity of multiheme cytochrome complex MtrCAB and their ability
78 to mediate micrometer-scale electron transport has been characterized in whole cells
79 (39), but no electrochemical characterization of OME/Vs has been reported that link
80 activity to multiheme cytochromes. Here, electrochemical measurements of isolated
81 OMVs were performed to determine if purified OMVs maintain the characteristic redox
82 features of the MtrCAB complex when detached from cells. Cyclic voltammetry (CV)
83 demonstrated redox activity of isolated membrane vesicles adhered to a gold electrode
84 via self-assembled monolayers (Fig. 1b). The first derivative (Fig. 1b inset) revealed a
85 prominent peak with a midpoint potential of 66 mV and a smaller peak at -25 mV versus

86 a standard hydrogen reference electrode (SHE). This midpoint potential is consistent with
87 the characteristics of multiheme cytochromes such as MtrC/OmcA from previous
88 microbial electrochemical studies (39, 40), suggesting that the extracellular redox
89 molecules of the cellular outer membrane extends to OMVs.

90 The proteome of the OMVs was compared to the proteome of purified outer
91 membranes extracted from whole cells. Using a label-free quantification method (41),
92 significant differences in the ratio of individual proteins in the vesicle to the outer
93 membrane could be computed (log fold change) (Fig 1c). The proteome of the purified
94 OMVs showed 328 proteins were significantly enriched in the vesicles as compared to
95 the outer membrane, and 314 proteins were significantly excluded from the vesicles (Fig.
96 1c, Supplemental table 1). MtrCAB cytochromes were present in the OMVs as well as
97 the outer membrane, supporting redox activity of OMVs observed by CV. Active protein
98 sorting into eukaryotic vesicles is a coordinated process involving protein sorting signal
99 recognition, localized membrane protein recruitment, initiation of membrane curvature
100 induction, and coating nascent vesicles with protein scaffolds (42). Several proteins
101 significantly enriched in the vesicles were identified that could contribute to OMV
102 formation, including the murein transglycosylase, the peptidoglycan degradation enzyme
103 holin, cell division coordinator CpoB, and a highly enriched putative BAR domain-
104 containing protein encoded by the gene at open reading frame SO_1507, hereafter
105 named BAR domain-like protein A (BdpA) (Fig. 1d).

106 Vesicle enrichment of BdpA led us to the hypothesis that BdpA could be involved
107 in membrane shaping of OMVs based on the role of BAR domain proteins in eukaryotes.
108 The C-terminal BAR domain of BdpA is predicted to span an alpha-helical region from AA

109 276-451 (E-value = 2.96e-03); however, since the identification of the protein is based on
110 homology to the eukaryotic BAR domain consensus sequence (cd07307), it is possible
111 that the BAR domain region extends beyond these bounds (Fig. 1d). Coiled coil prediction
112 (43) suggests BdpA exists in an oligomeric state of antiparallel alpha-helical dimers, as
113 is the case for all known BAR domain proteins (2, 44-46). The predicted structure of the
114 BAR domain-containing region generated in i-TASSER (47) shows a 3 helix bundle
115 (Supplemental Fig. 1a). When the BdpA BAR domain monomers were aligned to the
116 dimeric structure of the F-BAR protein Hof1p (48), the predicted dimer interface residues
117 of BdpA came into proximity, revealing an intrinsically curved dimer with positively
118 charged residues along the concave surface (Supplemental Fig. 1b). BdpA has a N-
119 terminal signal peptide with predicted cleavage sites between amino acids 22-23,
120 suggesting non-cytoplasmic localization (Fig. 1d). A galactose-binding domain-like
121 region positioned immediately downstream of the signal peptide supports lipid targeting
122 activity seen in other BAR domain proteins, such as the eukaryotic sorting nexins (49)
123 which have phox (PX) domains that bind phosphoinositides (50). The *S. oneidensis*
124 rough-type lipopolysaccharide (LPS) contains 2-acetamido-2-deoxy-D-galactose (51),
125 which suggests possible localization of the protein to the outer leaflet of the outer
126 membrane.

127 **BdpA controls size distribution of vesicles**

128 In eukaryotic cells, BAR domain proteins are implicated in vesicle formation (52,
129 53) and regulation of vesicle size (54). To determine whether BdpA influences vesicle
130 morphology, OMVs were harvested from wild type (WT) cells and cells in which the gene
131 for BdpA had been deleted (Δ*bdpA*), and their diameters were measured by dynamic light

132 scattering (DLS). WT OMVs had a median diameter of 190 nm with little variability in the
133 population (standard deviation (s.d.) = ±21 nm), while the diameters of Δ*bdpA* OMVs were
134 distributed over a wider range with a median value of 280 nm (s.d. = ± 131 nm (Fig 2a).
135 The data suggest BdpA controls vesicle diameter in membrane structures *ex vivo*,
136 potentially acting by stabilizing OMVs.

137 Cell-associated OMV frequency and size distribution was also measured in live
138 cultures using a perfusion flow imaging platform and the membrane stain FM 4-64, as
139 described previously (21). *S. oneidensis* strains were monitored for OME/V production
140 and progression over the course of 5 hours (>5 fields of view per replicate, n=3) using
141 time-lapse imaging. Spherical membrane stained extracellular structures were classified
142 as OMVs, while larger aspect ratio (i.e. length greater than the width) structures were
143 classified as OMEs. The proportion of cells producing 'large' vesicles, defined as having
144 a membrane clearly delineated from the interior of the vesicles and typically >300 nm,
145 was quantified, and Δ*bdpA* cells produced significantly more large vesicles compared to
146 WT cells (Fig. 2b) even though both the overall frequency of vesiculation and extensions
147 were the same (Fig. 2c). Previous studies showed that OMEs transition between large
148 vesicles and OMEs over time (21). BdpA appears to be involved in this transition in
149 *Shewanella* due to the increased frequency of large vesicles from Δ*bdpA* cells. The
150 median diameter of the OMVs is also the apparent maximum diameter observed in outer
151 membrane extensions (21) suggesting BdpA influences membrane morphologies of both
152 structures.

153 **BdpA constrains membrane extension morphology**

154 Cells were also visualized after deposition onto a glass coverslip instead of a
155 perfusion flow chamber as previously reported (20). BdpA was expressed from a 2,4-
156 diacetylphloroglucinol (DAPG)-inducible promoter (55) (P_{PhlF}-BdpA) in the Δ*bdpA* strain
157 containing the plasmid p452-*bdpA* with 12.5 μM DAPG. After 3 hours post deposition on
158 cover glass, OMEs can be seen extending from WT, Δ*bdpA*, and Δ*bdpA* p452-*bdpA* cells
159 (Fig. 3a, Supplemental Fig. 2, Supplemental videos 1-3, 5 fields of view, n=3). Similar to
160 perfusion flow experiments, no statistically significant difference in the overall frequency
161 of OME production was observed between the cells in static cultures. The resolution of
162 fluorescence microscopy was insufficient to identify morphological differences between
163 OMEs of wild type and mutant strains, therefore, cryo-TEM was used to assess OMEs in
164 each of the strains at the ultrastructural level.

165 *S. oneidensis* OMEs from unfixed WT, Δ*bdpA,* and Δ*bdpA* p452-*bdpA* strains were
166 visualized at 90 minutes (Supplemental Fig. 3) and 3 hours (Fig. 3a) following cell
167 deposition onto EM grids. By 3 hours post inoculation, images of WT cells consistently
168 show narrow, tubule-like OMEs or vesicle chains of symmetric curvature (Fig. 3b,c n=31
169 OMEs observed). The Δ*bdpA* OMEs appear as lobed, disordered vesicle chains with
170 irregular curvature compared to the WT ($p < 0.001$, Fisher's exact test), and vesicles can
171 be observed branching laterally from lobes on the extensions (Fig. 3b,c n=13 OMEs
172 observed). WT OMEs also exhibited lateral branching of vesicles and lobes, but they
173 exhibited uniform curvature and diameter between lobes, mirroring previous observations
174 of nascent OMEs imaged immediately following OME formation (21). Tubules were not
175 observed in any Δ*bdpA* OMEs at 3 hours (Fig. 3d). OMEs from Δ*bdpA* p452-*bdpA* cells

176 appear as narrow tubules of a uniform curvature or as ordered vesicle chains (Fig. 3b,c
177 n=3 OMEs observed), showing that expression of BdpA from a plasmid rescues the
178 mutant phenotype by constricting and ordering OMEs into narrow tubules and chains (Fig.
179 3d, $p < 0.01$, Fisher's exact test). Earlier in OME progression at 90 minutes, WT OME
180 phenotypes appeared narrow, tubule-like, and seldom interspersed with lobed regions
181 (Supplemental figure 3a). In Δ*bdpA* OMEs, lobed regions are prevalent with irregular
182 curvature (Supplemental figure 3b). Several narrow Δ*bdpA* p452-*bdpA* OMEs evenly
183 interspersed with slight constriction points or "junction densities" were observed extending
184 from a single cell (Supplemental Fig. 3c).

185 **Expression of BdpA results in OMEs during planktonic growth**

186 *S. oneidensis* OMEs are more commonly observed in surface attached cells than
187 planktonic cells (20, 21). BAR domain proteins can directly promote tubule formation from
188 liposomes *in vitro*(9), so inducing expression of an additional copy of the *bdpA* gene prior
189 to attachment could result in OME formation even during planktonic growth. Growth
190 curves were similar in cultures with the pBBR1-mcs2 empty vector in either of the WT or
191 Δ*bdpA* background strains, but induction of *bdpA* in Δ*bdpA* p452-*bdpA* cells at higher
192 concentrations of 1.25 and 12.5 μM 2,4-diacetylphloroglucinol affected the growth rate
193 (Supplemental figure 4). Planktonic cultures inoculated from overnight cultures were
194 induced with 12.5 μM DAPG for 1 hour, labeled with FM 4-64, and imaged by confocal
195 microscopy. Neither WT (Fig. 4) nor WT with the empty plasmid exposed to 12.5 μM
196 DAPG (not shown) displayed OMEs immediately following deposition onto cover glass.
197 However, 12.5 μM DAPG-induced bdpA expression from p452-*bdpA* in the WT
198 background strain (WT p452-*bdpA*) displayed OMEs immediately, ranging between 1-7

199 extensions per cell (Figure 4, Supplemental video 4). The abundance of OMEs suggest
200 that increased *bdpA* expression in planktonic cultures can initiate membrane sculpting
201 into OMEs at the expense of cell division.

202 The ultrastructure of OMEs resulting from expression of *bpdA* from WT p452-*bdpA*
203 cells was examined by cryo-TEM, but in this case samples from planktonic cultures were
204 vitrified on EM grids after induction rather than incubation during induction on the EM
205 grids. By expressing extra copies of *bdpA* in the WT strain during planktonic induction,
206 we predicted that OME morphology would be predominately reliant on curvature
207 formation by BdpA rather than other unidentified structural proteins involved in intrinsic
208 OME formation. OMEs appear as tubule-like segments interspersed with pearled regions
209 proximal to the main cell body (Fig. 4b). OMEs from the MR-1 p452-*bdpA* strain are
210 observed as thin, tubule-like outer membrane vesicle chains, suggesting BdpA
211 involvement in the constriction of the larger outer membrane vesicle chains into longer,
212 tubule-like extensions with more evenly interspersed junction densities. The BdpA OME
213 phenotype more closely resembles membrane tubules formed by the F-BAR protein
214 Pacsin1 from eukaryotic cells, showing a mixture of tubule regions interspersed with
215 pearled segments (56, 57). Orientation and association of Pacsin1 dimers on the
216 membrane surface with one another impacted tubule morphology, and BdpA membrane
217 sculpting could be similar mechanistically.

218 **BdpA-mediated membrane extensions in *Marinobacter atlanticus* CP1 and *E. coli*.**

219 To test the effect of expressing BdpA in an organism with no predicted BAR
220 domain-containing proteins and no apparent OME production, BdpA was expressed in
221 *Marinobacter atlanticus* CP1 (58). *Marinobacter* and *Shewanella* are of the same

222 phylogenetic order (*Alteromonadales*) and have been used for heterologous expression
223 of other *S. oneidensis* proteins, such as MtrCAB (59, 60). Upon exposure to DAPG, *M.*
224 *atlanticus* containing the p452-*bdpA* construct (CP1 p452-*bdpA*) forms membrane
225 extensions (Figure 4). OMEs ranged from small membrane blebs to OME tubules
226 extending up to greater than 10 μm in length from the surface of the cell (Supplemental
227 Fig. 5). As noted previously, variation in the tubule phenotypes are commonly seen in
228 tubules from eukaryotic F-BAR proteins (56, 57), showing possible mechanistic overlap
229 of membrane curvature functionalities between these two separate BAR domain proteins.

230 In previous membrane curvature formation experiments with eukaryotic BAR
231 domain proteins, localized BAR domain protein concentrations affected the resultant
232 shape of the membranes, ranging from bulges to tubules and branched, reticular tubule
233 networks at the highest protein densities (61-63). We predicted that expression of BdpA
234 in cells optimized for protein overexpression, such *E. coli* BL21(DE3), would show OMEs
235 resembling BAR protein concentration-dependent structures previously observed from
236 eukaryotic BAR protein experiments *in vitro*. While the uninduced *E. coli* BL21(DE3)
237 p452-*bdpA* cells had uniform, continuous cell membranes similar to those of plasmid-free
238 BL21(DE3) cells under the conditions tested, *E. coli* BL21(DE3) cells containing the p452-
239 *bdpA* vector induced with 12.5 μM DAPG had outer membrane extensions and vesicles
240 (Figure 4). When visualized over time, OMEs progressed towards a network of reticular
241 membrane structures extending from the cell (Fig. 4c). After 30 minutes, additional
242 membrane blebs were observed that developed into elongated OMEs by 60 minutes.
243 Growth of *E. coli* OMEs was coincident with shrinking of the cell body (from initial cell
244 length = 4.5 μm to 3.5 μm at 60 minutes), supporting direct membrane sculpting activity

245 of BdpA. *In vitro* tubule formation assays with purified proteins and liposomes are the
246 canonical approach by which eukaryotic BAR domain proteins have been assessed for
247 membrane sculpting activity. However, molecular crowding of purified proteins with no
248 documented membrane curvature formation activity, such as GFP, can also lead to
249 ordering of liposomes into tubules (64). Further, tubule formation from liposomes is not
250 limited to BAR domain protein activity and requires non-physiologically high protein
251 concentrations (65-67). The heterologous expression approach allows for more rapid
252 screening of putative BAR domain proteins for membrane sculpting activity, avoiding the
253 need for protein purification and *in vitro* systems.

254 **P-BAR: a new BAR domain subtype**

255 The discovery of a novel, functional BAR domain protein in prokaryotes provokes
256 questions into the evolutionary origin of BAR domains, such as whether the BdpA BAR
257 domain in *S. oneidensis* arose as a result of convergent evolution, a horizontal gene
258 transfer event, or has a last common ancestor across all domains of life. BdpA homologs
259 were identified by PSI-BLAST in other *Gammaproteobacteria*, including most but not all
260 species of *Shewanella*, as well as *Alishewanella*, *Rheinheimera*, and *Cellvibrio*
261 (Supplemental Fig. 6). The current BAR domain Pfam Hidden Markov Model (HMM)
262 prediction analysis identified BAR domain features in only 5 of the 52 prokaryotic
263 homologs despite greater than 90% homology to *S. oneidensis* BdpA. An amino acid
264 alignment of the 52 BdpA homologs was used to generate a maximum likelihood
265 phylogenetic tree showing evolutionary relatedness of BdpA orthologs to the BAR domain
266 prediction sequences (Supplemental Fig. 6). The 5 BdpA orthologs predicted to contain
267 a BAR domain based on the current model were subsequently aligned with representative

268 known BAR proteins from the various BAR domain subtypes (N-BAR, F-BAR, and I-
269 BAR)(68). BdpA and its prokaryotic orthologs cluster separately from the eukaryotic BAR
270 proteins in their own distinct clade (Fig. 5), suggesting that while BdpA contains a
271 functional BAR domain, it represents its own class of BAR domain, hereafter named P-
272 BAR (Prokaryotic BAR). The closest phylogenetic relative to P-BAR domains are the F-
273 BAR domains, and BdpA membrane sculpting phenotypes are functionally similar to
274 previous *in vitro* observations from Pacsin1 (56, 57). It is possible that the P-BAR domain
275 arose as a result of horizontal gene transfer from a eukaryote due to the prevalence of
276 eukaryotic coiled-coil proteins with predicted homology to BdpA after 2 iterations of PSI-
277 BLAST. However, the branch lengths and low bootstrap values supporting the placement
278 of P-BAR relative to other BAR domain subtypes make it challenging to directly infer the
279 evolutionary history of P-BAR domains. Discovery of other putative P-BAR proteins
280 would help to build this analysis, and if future comparative proteomics analysis of OME/Vs
281 demonstrates overlapping activity of BdpA with preferential cargo loading into OME/Vs, it
282 could hint at the evolutionary origins of vesicle-based protein trafficking. Conservation of
283 BAR domain proteins supports the notion that three-dimensional organization of proteins
284 in lipid structures is as important to prokaryotes as it is eukaryotes, and suggests
285 additional novel P-BAR proteins are waiting to be discovered.

286 **Conclusion**

287 *S. oneidensis* expresses a functional prokaryotic BAR domain protein, which is the
288 first identified and characterized in bacteria. Enrichment of BdpA in the redox-active
289 OMVs suggests overlapping mechanistic functionality with eukaryotic BAR proteins in the
290 context of vesicle constriction (52). This finding was further demonstrated through

291 fluorescence microscopy during perfusion flow, where large vesicles were more
292 frequently observed from Δ*bdpA*. Membrane constriction activity of BdpA was confirmed
293 through cryo-EM images that depicted an inability to transition into ordered tubules in the
294 absence of *bdpA* expression. Variation in OMEs with BdpA ranged from ordered, narrow
295 vesicle chains of a consistent diameter to stable tubules. The closest phylogenetic
296 eukaryotic BAR domain subtype to BdpA, F-BAR domains, exhibit similar variation in
297 tubule morphology, depending upon the orientation of the tip-to-tip oligomerization around
298 the tubules (2, 3, 57). Subsequent studies will include vesicle constriction into tubules
299 with purified protein to ascertain the extent of functional mechanistic similarity of BdpA to
300 other F-BAR proteins. However, heterologous expression of BdpA and other potential P-
301 BAR domain proteins enables rapid validation of membrane sculpting mechanistic
302 activity. Ultimately, the discovery of BdpA and its homologs presents a critical first step in
303 the new field of bacterial BAR domain protein research.

304 **Methods**

305 **Bacterial strains, plasmids, and medium** The bacterial strains used in this study can
306 be found in Supplemental Table 1. *S. oneidensis* strains were grown aerobically in Luria
307 Bertani (LB) media at 30˚C with 50 µg/mL kanamycin when maintaining the plasmid. To
308 observe membrane extensions, cells were centrifuged and resuspended in a defined
309 media comprised of 30 mM Pipes, 60 mM sodium DL-lactate as an electron donor, 28mM
310 NH_4Cl, 1.34 mM KCl, 4.35 mM NaH_2PO_4, 7.5 mM NaOH, 30 mM NaCl, 1mM $MgCl_2$, 1
311 mM $CaCl_2$, and 0.05 mM ferric nitrilotriacetic acid(22). *Marinobacter atlanticus* CP1
312 strains were grown in BB media (50% LB media, 50% Marine broth) at 30˚C with 100
313 µg/mL kanamycin to maintain the plasmids as described previously (58).

314 Inducible BdpA expression plasmids were constructed for use in *S. oneidensis*
315 MR-1, *M. atlanticus* CP1, and *E. coli* BL21(DE3) using the pBBR1-mcs2 backbone
316 described previously (58). The Marionette sensor components (*phlF* promoter,
317 consitutively expressed PhlF repressor, and yellow fluorescence protein (YFP)) cassette
318 from pAJM.452 (55) was cloned into the pBBR1-mcs2 backbone, and the YFP cassette
319 was replaced with the gene encoding BdpA by Gibson assembly (primers in
320 Supplemental Table 2). The resulting plasmid was given the name p452-*bdpA*. The
321 Gibson assembly reactions were electroporated into *E. coli* Top10 DH5α cells
322 (Invitrogen), and the sequences were confirmed through Sanger sequencing (Eurofins
323 genomics). Plasmid constructs were chemically transformed into conjugation-competent
324 *E. coli* WM3064 cells for conjugative transfer into the recipient bacterial strains of *S.*
325 *oneidensis* MR-1 and *M. atlanticus* CP1. The same BdpA expression vector was
326 transformed into *E. coli* BL21(DE3) cells (Invitrogen) by chemical transformation.

327 Generation of a scarless *ΔbdpA* knockout mutant of *S. oneidensis* was performed
328 by combining 1 kilobase fragments flanking upstream and downstream from *bdpA* by
329 Gibson assembly into the pSMV3 suicide vector. The resultant plasmid pSMV3_1507KO
330 was transformed into *E. coli* DH5α λ*pir* strain UQ950 cells for propagation. Plasmid
331 sequences were confirmed by Sanger sequencing before chemical transformation into *E.*
332 *coli* WM3064 for conjugation into *S. oneidensis*. Conjugation of pSMV3_1507KO into *S.*
333 *oneidensis* MR-1 was performed as described previously (23). Optical densities at 600nm
334 were measured to determine growth curves for each strain in either LB or SDM with 50
335 µg/mL kanamycin and 2,4-diacetylphloroglucinol (DAPG) as indicated. Cultures of 500
336 µL samples diluted to an initial OD_{600} of 0.1 were grown in Costar® polystyrene 48 well
337 plates (Corning Incorporated) within a Tecan Infinite M1000 Pro (Grödig, Austria) plate
338 reader at 30°C with shaking agitation at 258 rpm. Optical densities were recorded every
339 15 minutes with i-Control software (2.7). All measurements were performed in triplicate.

340 **Purification of Outer Membrane Vesicles** *S. oneidensis* MR-1 cells were grown in LB
341 in 1L non-baffled flasks at 30° C at 200 RPM. When an OD_{600} of 3.0 was reached, cells
342 were pelleted by centrifugation at 5000 x g for 20 min at 4°C, resulting supernatant was
343 filtered through a 0.45 µm filter to remove remaining bacterial cells. Vesicles were
344 obtained by centrifugation at 38,400 x g for 1 h at 4°C in an Avanti J-20XP centrifuge
345 (Beckman Coulter, Inc). Pelleted vesicles were resuspended in 20 ml of 50 mM HEPES
346 (pH 6.8) and filtered through 0.22 µm pore size filters. Vesicles were again pelleted as
347 described above and finally resuspended in 50 mM HEPES, pH 6.8, except for vesicle
348 preparations used for electrochemistry which were suspended in 100 mM MES, 100 mM

349 KCl, pH 6.8. Extracellular DNA, flagella, and pili can all be co-purified. Protocol was
350 adapted from Perez-Cruz et al (69).

351 **Cryoelectron tomography** Vesicle samples were diluted to a protein concentration of
352 0.4 mg/mL and applied to glow-discharged, X-thick carbon-coated, R2/2, 200 mesh
353 copper Quantifoil grid (Quantifoil Micro Tools) using a Vitrobot chamber (FEI). Grids were
354 automatically plunge frozen and saved for subsequent imaging. No fixative was used.
355 Images were collected on an FEI Krios transmission electron microscope equipped with
356 a K2 Summit counting electron-detector camera (Gatan). Data were collected using
357 customized scripts in SerialEM(70), with each tilt series ranging from −60° to 60° in 3°
358 increments, an underfocus of ∼1-5 µm, and a cumulative electron dose of 121 e/A^2 for
359 each individual tilt series. Tomograms were reconstructed using a combination of ctffind4
360 (71) and the IMOD software package (72).

361

362 **Dynamic Light Scattering** Distributions of vesicle diameters were measured with Wyatt
363 Technology's Möbiuζ dynamic light scattering instrument with DYNAMICS software for
364 data collection and analysis. Data was collected using a 0-50 mW laser at 830 nm. The
365 scattered photons were detected at 90˚. Measurements were recorded from 11 biological
366 replicates for WT OMVs, and 9 replicates for Δ*bdpA* OMVs. Mobius software analyzed
367 the population of particles to generate a table with binned diameters and the percentage
368 of particles at each diameter. In order to compute the average vesicle size from each
369 sample, a weighted average was computed so that diameter bins that had the most
370 number of vesicles would be accurately represented in the final average weight of the
371 population. The product of each diameter is multiplied by its percentage in the population,
372 these products are added together for each sample, divided by the sum of weights. The

373 weighted diameters per replicate were then averaged for each genotype. Statistical
374 significance was determined by Student's *t*-test, and error bars represent standard
375 deviation.

376 **Electrochemistry** CHA Industries Mark 40 e-beam and thermal evaporator was used to
377 deposit a 5 nm Ti adhesion layer and then a 100 nm Au layer onto cleaned glass
378 coverslips (43mm x 50mm #1 Thermo Scientific Gold Seal Cover Glass, Portsmouth NH,
379 USA). Self-assembled monolayers were formed by incubated the gold coverslip in a
380 solution of 1mM 6-mercaptohexanoic acid in 200 proof ethanol for at least 2 hours.
381 Electrode was then rinsed several time in ethanol followed by several rinses in milliQ
382 water. The SAMs layer was then activated by incubation in 100 mM N-(3-
383 Dimethylaminopropyl)-N′-ethylcarbodiimide hydrochloride and 25 mM N-
384 hydroxysuccinimide, pH 4, for 30 minutes. A sample of outer membrane vesicles was
385 deposited on the surface of the electrode and incubated at room temperature overnight
386 in a humid environment. Cyclic voltammetry was performed in a 50 mL three-electrode
387 half-cell completed with a platinum counter electrode, and a 1 M KCl Ag/AgCl reference
388 electrode electrical controlled by a Gamry 600 potentiostat (Gamry, Warminster, PA).
389 The whole experiment was completed in an anaerobic chamber with 95% nitrogen, 5%
390 hydrogen atmosphere.

391 **Proteomics** Vesicle samples were prepared as described above. *S. oneidensis* outer
392 membrane (OM) was purified via the Sarkosyl method described by Brown et al.(73). A
393 50 mL overnight culture of cells was harvested by centrifugation at 10,000 × g for 10 min.
394 The cell pellet suspended in 20 mL of 20 mM ice-cold sodium phosphate (pH 7.5) and
395 passed four times through a French Press (12000 lb/in^2). The lysate was centrifuged at
396 5,000 × g for 30 min to remove unbroken cells. The remaining supernatant was
397 centrifuged at 45,000 × g for 1 h to pellet membranes. Crude membranes were
398 suspended in 20 mL 0.5% Sarkosyl in 20 mM sodium phosphate and shaken horizontally
399 at 200 rpm for 30 min at room temperature. The crude membrane sample was centrifuged
400 at 45,000 × g for 1 h to pellet the OM. The pellet of OM was washed in ice-cold sodium
401 phosphate and recentrifuged.

402 To prepare for mass spectrometry samples were treated sequentially with urea,
403 TCEP, iodoactinamide, lysl endopeptidase, trypsin, and formic acid. Peptides were then
404 desalted by HPLC with a Microm Bioresources C8 peptide macrotrap (3x8mm). The
405 digested samples were subjected to LC-MS/MS analysis on a nanoflow LC system,
406 EASY-nLC 1200, (Thermo Fisher Scientific) coupled to a QExactive HF Orbitrap mass
407 spectrometer (Thermo Fisher Scientific, Bremen, Germany) equipped with a Nanospray
408 Flex ion source. Samples were directly loaded onto a PicoFrit column (New Objective,
409 Woburn, MA) packed in house with ReproSil-Pur C18AQ 1.9 um resin (120A° pore size,
410 Dr. Maisch, Ammerbuch, Germany). The 20 cm x 50 µm ID column was heated to 60°
411 C. The peptides were separated with a 120 min gradient at a flow rate of 220 nL/min.
412 The gradient was as follows: 2–6% Solvent B (7.5 min), 6-25% B (82.5 min), and 25-40%
413 B (30 min) and to 100% B (9min). Solvent A consisted of 97.8% H2O, 2% acetonitrile,

414 and 0.2% formic acid and solvent B consisted of 19.8% H2O, 80% ACN, and 0.2% formic
415 acid. The QExactive HF Orbitrap was operated in data dependent mode with the Tune
416 (version 2.7 SP1build 2659) instrument control software. Spray voltage was set to 2.5
417 kV, S-lens RF level at 50, and heated capillary at 275 °C. Full scan resolution was set to
418 60,000 at m/z 200. Full scan target was 3 × 106 with a maximum injection time of 15 ms.
419 Mass range was set to 300−1650 m/z. For data dependent MS2 scans the loop count
420 was 12, target value was set at 1 × 105, and intensity threshold was kept at 1 × 105.
421 Isolation width was set at 1.2 m/z and a fixed first mass of 100 was used. Normalized
422 collision energy was set at 28. Peptide match was set to off, and isotope exclusion was
423 on. Data acquisition was controlled by Xcalibur (4.0.27.13) and all data was acquired in
424 profile mode.

425 **Bioinformatics** Putative BAR domain SO_1507 (BdpA) was identified in search of
426 annotation terms of *S. oneidensis* MR-1. The conserved domain database (CDD-
427 search)(NCBI) was accessed to identify the position-specific scoring matrix (PSSM) of
428 the specific region of SO_1507 that represented the BAR domain (amino acid residues
429 at positions 276-421). The domain prediction matched to BAR superfamily cl12013 and
430 specifically to the family member BAR cd07307. LOGICOIL multi-state coiled-coil
431 oligomeric state prediction was used to predict the presence of coiled-coils within BdpA
432 (43). SignalP 6.1 was used to detect the presence of the signal peptide and cellular
433 localization of BdpA (74). I-TASSER protein structure prediction (47) was used to
434 generate a predicted model of the BAR domain region of BdpA. Alignment of the predicted
435 BdpA BAR domain structure model to the structure of Hof1p was performed in the PyMOL
436 Molecular Graphics System, Version 2.0 (Schrödinger, LLC).

437 A PSI-BLAST (75) search against the NCBI nr database was performed using the
438 BdpA BAR sequence as the initial search seed to determine how prevalent the BdpA BAR
439 domain is in related species. Conserved BdpA orthologs were annotated as hypothetical
440 proteins in all of the species identified. In the initial round, 24 proteins were found from
441 other organisms identified as *Shewanella* with a high conservation among the proteins
442 and another 28 proteins were found in more distant bacteria species that had similarity of
443 65% to 44%. A second iteration identified a few proteins much more distantly related from
444 bacterial species and then proteins from eukaryote phylum *Arthropoda* that were
445 annotated as being centrosomal proteins. All of the found proteins from bacterial species
446 were hypothetical proteins with no known function. Only five of the proteins from the
447 search returned hits to the PSSM of the BAR cd07307. The identity among the proteins
448 was very high and examination of the proteins suggests that a functional form similar to
449 the BAR domain would result for all the found proteins. Overall, this places BdpA as a
450 protein that just barely meets criteria via PSSM models to be assigned as matching the
451 BAR domain while the rest of the proteins found have enough differences to fail to match
452 the BAR model while still being very similar to BdpA. An attempt was made to build up a
453 HMM (Hidden Markov Model) using hmmer (76) to use for searching for other proteins
454 that might match, but as with the PSI-BLAST search, only the proteins that formed the
455 model returned as good matches. There appears to be a tight clade of very similar
456 proteins with very little differentiation in the sequence. This indicates that while sequence
457 homology between BdpA and the existing BAR domain consensus sequence predicted
458 the BAR domain region in BdpA using hmmer or NCBI tools, the sequence conservation
459 is at the cusp of a positive hit by the HMM since other closely related (>90% homology)

460 BdpA orthologs were not predicted to contain a BAR domain by this method. The most
461 homologous eukaryotic protein to BdpA (27%) is a putative centrosomal protein in
462 *Vollenhovia emeryi* (accession #: XP_011868153) that is predicted to contain an amino
463 terminal C2 membrane binding domain and a carboxy-terminal SMC domain within a
464 coiled-coil region. Despite CDD search failing to predict the presence of a BAR domain
465 in this protein, it does not preclude the presence of one, pending an updated BAR Pfam
466 HMM. Alignments and phylogenies were constructed in MEGA 7. MUSCLE was used to
467 align protein sequences, and Maximum Likelihood phylogenies were inferred using the
468 Le-Gascuel (LG+G) substitution matrix (77). Initial trees for the heuristic search were
469 obtained automatically by applying Neighbor-Join and BioNJ algorithms to a matrix of
470 pairwise distances estimated using a JTT model, and then selecting the topology with
471 superior log likelihood value. A discrete Gamma distribution was used to model
472 evolutionary rate differences among sites as indicated in figure legends. All positions with
473 less than 85% site coverage were eliminated.

474 **Confocal microscopy** For *in vivo* imaging of intrinsic outer membrane extension
475 production, *S. oneidensis* MR-1 strains were grown in LB media overnight, washed twice
476 with SDM, and diluted to an OD_{600} of 0.05 in 1 mL of SDM with appropriate antibiotics.
477 Prior to pipetting, ~1cm of the pipette tip was trimmed to minimize shear forces during
478 transfer. 100 µL of each culture was labeled with 1 µL 1M FM 4-64 to visualize the cell
479 membranes. After staining, 10 µL of the labeled cell suspension was gently pipetted onto
480 22 x 22 mm No.1 cover glass (VWR) and sealed onto glass slides with clear acrylic nail
481 polish for confocal imaging or onto Lab-Tek chambered #1 cover glass (Thermo Fischer
482 Scientific)(for widefield fluorescence). On average, intrinsic membrane extension

483 formation could be observed starting after 45 minutes sealed onto cover glass. For
484 planktonic OME production from BdpA induction in trans, diluted cells (in either SDM for
485 *S. oneidensis*, BB for *M. atlanticus*, or LB for *E. coli*) were induced with 12.5 μM DAPG
486 for 1 hour at 30˚C with 200 RPM shaking agitation. Cells were labeled with FM 4-64 and
487 sealed onto glass slides as before. Induced OMEs were imaged immediately after
488 mounting onto slides.

489 Confocal images were taken by a Zeiss LSM 800 confocal microscope with a Plan-
490 Apochromat 63x/1.4 numerical aperture oil immersion M27 objective. FM 4-64
491 fluorescence was excited at 506 nm: 0.20% laser power. Emission spectra was detected
492 from 592-700 nm using the LSM 800 GaAsP-Pmt2 detector. To capture the dynamics of
493 the OMEs, images were collected over the designated length of time between 0.27 – 0.63
494 seconds per frame. Single frame time series images were collected of either a 50.71 μm
495 by 50.71 μm (2x zoom) or a 20.28 μm by 20.28 μm (5x zoom) field of view. Widefield
496 fluorescence images were taken using a LED-Module 511 nm light source at 74.2%
497 intensity with 583-600 nm filters and a 91 He CFP/YFP/mCherry reflector. Excitation and
498 emission spectra were 506 nm and 751 nm, respectively. Images were collected using a
499 Hamamatsu camera with a 250 ms exposure time. Images were recorded using the Zeiss
500 Zen software (Carl Zeiss Microscopy, LLC, Thornwood, NY, USA). Frequency of OMEs
501 was calculated from 3 biological replicates of each strain from at least 5 fields of view
502 selected at random (2444 cells from WT, 4378 from Δ*bdpA*, and 3354 from Δ*bdpA* p452-
503 *bdpA*). OMEs were counted per cell per field of view from a 20 second video if a
504 membrane extension was observed extending from the cell over that timeframe.
505 Statistical significance was determined by two-tailed Student's *t*-test.

506 **Perfusion flow microscopy** For OME statistics comparing *S. oneidensis* strains MR-1
507 and Δ*bdpA,* cells were pre-grown aerobically from frozen (-80°C) stock in 10 mL of Luria-
508 Bertani (LB) broth (supplemented with 50 µg/mL Kanamycin for strains with plasmid) in a
509 125-mL flask overnight at 30°C and 225 rpm. The next day, the stationary phase (OD_{600}
510 3.0 – 3.3) preculture was used to inoculate 1:100 into 10 mL of fresh LB medium in a 125-
511 mL flask. After ~6 hours at 30°C and 225 rpm, when the OD_{600} was 2.4 (late log phase),
512 5 mL of cells were collected by centrifugation at 4226 x *g* for 5 min and washed twice in
513 defined medium. The perfusion chamber, microscope, and flow medium described
514 previously (20-22) were used for all perfusion flow OME statistics experiments. During
515 each 5 hour imaging experiment, the perfusion chamber was first filled with this flow
516 medium, then <1 mL of washed cells were slowly injected for a surface density of ~100-
517 300 cells per 112 x 112 µm field of view on a Nikon Eclipse Ti-E inverted microscope with
518 the NIS-Elements AR software. Cells were allowed to attach for 5-15 minutes on the
519 coverslip before perfusion flow was resumed at a volumetric flow rate of 6.25 ± 0.1 µL/s.
520 Cells and OMEs were visualized with the red membrane stain FM 4-64FX in the flow
521 medium (0.25 µg/mL of flow medium). A total of 1,831 wild type and 2,265 Δ*bdpA* cells
522 were used for extension and vesicle quantification. Experiments were performed from
523 three individual biological replicates for each strain, and statistical significance was
524 determined by two-tailed χ^2 test.

525 **Cryo transmission electron microscopy**

526 *Shewanella* strains were streaked onto LB plates with or without kanamycin and allowed
527 to incubate 3 days on a benchtop. The night before freezing, individual colonies were
528 inoculated into 3 ml LB +/- kanamycin and incubated at 30 °C overnight with 200 rpm

529 shaking. The following morning optical densities of the cultures were measured at
530 600nm and adjusted to a final OD_{600} of 1. Cells were pelleted at 8,000 rpm for three
531 minutes for buffer exchange/washes. For the Δ*bdpA* p452-*bdpA* transformed cells, 12.5
532 μM DAPG was added. A freshly glow discharged 200 mesh copper grid with R2/1
533 Quantifoil carbon film was placed into a concavity slide. Approximately 150 μl of a 1:10
534 dilution of the cell suspensions, with or without the inducer, was added to cover the grid.
535 A glass coverslip was then lowered onto the concavity to exclude air bubbles. The
536 edges of the coverslip were then sealed with nail polish to prevent media evaporation.
537 The slide assembly was then incubated in a 30 °C incubator for 1.5 to 3 hours.
538 Immediately prior to plunge freezing, the top coverslip was removed by scoring the nail
539 polish with a razor blade. TEM grids with cells were gently retrieved with forceps and
540 loaded into a Leica grid plunge for automated blotting and plunging into LN_2-cooled
541 liquid ethane. Vitrified grids were transferred to a LN_2 storage dewar. Imaging of frozen
542 samples was performed on either a Titan (ThermoFisher Scientific) microscope
543 equipped with a Gatan Ultrascan camera and operating at 300 kV or a Talos
544 (ThermoFisher Scientific) equipped with a Ceta camera and operating at 200 kV.
545 Images were acquired at 10,000x to 20,000x magnification and were adjusted by
546 bandpass filtering. Unfixed OMEs were sorted based on appearance into 4 categories.
547 Tubules were narrow OMEs with relatively uniform or slight symmetric curvature.
548 Narrow chains were recorded as OMEs with a narrow, consistent diameter and
549 symmetric curvature at constriction points. Irregular chains were classified as OMEs
550 without a consistent diameter throughout the length of the OME and asymmetric
551 curvature on either side of the extension. Blebs \ bulges were outer membrane

552 structures that did not resemble OMEs but still extended from the cell membrane
553 surface. Phenotypes were documented from observations of 31 WT, 13 Δ*bdpA*, and 3
554 Δ*bdpA* p452-*bdpA* OMEs over three separate biological replicates, with two technical
555 replicates of each strain per biological replicate. Two-tailed statistical significance
556 between strains was calculated by Fisher's exact test with the Freeman-Halton
557 extension for a 2x4 matrix (78) using the Real Statistics Resource Pack software
558 (Release 6.8).

559

560 **Acknowledgements**

561 We thank Dr. Jeffery Gralnick for helpful discussions and advice; Dr. Adam Meyer
562 and Dr. Chris Voigt for the DAPG-inducible Marionette promoter; Dr. Annie Moradian and
563 Dr. Mike Sweredoski and the California Institute of Technology Proteome Exploration Lab
564 for useful discussions on the preparation and analysis of proteomics data. Some of the
565 cryo-TEM work was done in the Beckman Institute Resource Center for Transmission
566 Electron Microscopy at Caltech. This work was supported by the United States
567 Department of Defense Synthetic Biology for Military Environments (SBME) Applied
568 Research for the Advancement of Science and Technology Priorities (ARAP) program.
569 Work in ME-N's lab was supported by the U.S. Office of Naval Research Multidisciplinary
570 University Research Initiative Grant No. N00014-18-1-2632. LAZ was partially supported
571 by the National Science Foundation grant DEB-1542527. SX was supported by the
572 Division of Chemical Sciences, Geosciences, and Biosciences, Office of Basic Energy
573 Sciences of the U.S. Department of Energy through grant DE-FG02-13ER16415. Work
574 in GJJ's lab was supported by the National Institute of Health (GM122588 to GJJ).

575 **Author Contributions**

576 DP and LZ conceived the study independently then combined projects when
577 complementary data on BdpA was discovered. LZ purified OMVs, prepared samples for
578 LC MS-MS, and performed DLS measurements. LZ and SX made electrochemical
579 measurements and analysis. DP conducted BdpA domain prediction and validation
580 analysis, generated the p452-*bdpA* plasmid, Δ*bdpA* and p452-*bdpA* strains. DP and GC
581 conducted fluorescence imaging experiments, and DP, LZ, and GC analyzed the data.
582 LB adapted the Marionette sensor (P_{phlF}-YFP) into pBBR1-mcs2. LZ and LAM performed
583 cryo-TEM of OMVs. GC and LZ analyzed perfusion flow system data. CH, DP, and LD
584 performed cryo-TEM experiments of OMEs and image processing / analysis. DP and AM
585 generated phylogenetic data, and DP, AM, and BE analyzed the data. DP, LZ, CM, GC,
586 AM, LAM, BE, GJJ, LD, MEN, and SG provided data interpretation. DP, LZ, MEN, and
587 SG wrote the manuscript, with input from all coauthors.

588

589 ## References

590 1. Peter BJ*, et al.* (2004) BAR domains as sensors of membrane curvature: the amphiphysin BAR
591 structure. *Science* 303(5657):495-499.
592 2. Frost A, De Camilli P, & Unger VM (2007) F-BAR proteins join the BAR family fold. *Structure*
593 15(7):751-753.
594 3. Shimada A*, et al.* (2007) Curved EFC/F-BAR-domain dimers are joined end to end into a filament
595 for membrane invagination in endocytosis. *Cell* 129(4):761-772.
596 4. Weissenhorn W (2005) Crystal structure of the endophilin-A1 BAR domain. *J. Mol. Biol.*
597 351(3):653-661.
598 5. Drin G & Antonny B (2010) Amphipathic helices and membrane curvature. *FEBS Lett.*
599 584(9):1840-1847.
600 6. Seet LF & Hong W (2006) The Phox (PX) domain proteins and membrane traffic. *Biochim.*
601 *Biophys. Acta* 1761(8):878-896.
602 7. Itoh T & De Camilli P (2006) BAR, F-BAR (EFC) and ENTH/ANTH domains in the regulation of
603 membrane-cytosol interfaces and membrane curvature. *Biochim. Biophys. Acta* 1761(8):897-
604 912.
605 8. Knaevelsrud H*, et al.* (2013) Membrane remodeling by the PX-BAR protein SNX18 promotes
606 autophagosome formation. *J. Cell Biol.* 202(2):331-349.
607 9. Simunovic M, Voth GA, Callan-Jones A, & Bassereau P (2015) When Physics Takes Over: BAR
608 Proteins and Membrane Curvature. *Trends Cell Biol.* 25(12):780-792.
609 10. Mim C*, et al.* (2012) Structural basis of membrane bending by the N-BAR protein endophilin. *Cell*
610 149(1):137-145.
611 11. Habermann B (2004) The BAR-domain family of proteins: a case of bending and binding? *EMBO*
612 *reports* 5(3):250-255.
613 12. Miki H, Yamaguchi H, Suetsugu S, & Takenawa T (2000) IRSp53 is an essential intermediate
614 between Rac and WAVE in the regulation of membrane ruffling. *Nature* 408(6813):732-735.
615 13. Carman PJ & Dominguez R (2018) BAR domain proteins-a linkage between cellular membranes,
616 signaling pathways, and the actin cytoskeleton. *Biophys Rev* 10(6):1587-1604.
617 14. Toyofuku M, Nomura N, & Eberl L (2018) Types and origins of bacterial membrane vesicles.
618 *Nature Reviews Microbiology*.
619 15. Remis JP*, et al.* (2014) Bacterial social networks: structure and composition of Myxococcus
620 xanthus outer membrane vesicle chains. *Environ. Microbiol.* 16(2):598-610.
621 16. Wei X, Vassallo CN, Pathak DT, & Wall D (2014) Myxobacteria produce outer membrane-
622 enclosed tubes in unstructured environments. *J. Bacteriol.* 196(10):1807-1814.
623 17. Fischer T*, et al.* (2019) Biopearling of Interconnected Outer Membrane Vesicle Chains by a
624 Marine Flavobacterium. *Appl. Environ. Microbiol.* 85(19).
625 18. Hampton CM*, et al.* (2017) The Opportunistic Pathogen Vibrio vulnificus Produces Outer
626 Membrane Vesicles in a Spatially Distinct Manner Related to Capsular Polysaccharide. *Front.*
627 *Microbiol.* 8:2177.
628 19. Sampath V, McCaig WD, & Thanassi DG (2018) Amino acid deprivation and central carbon
629 metabolism regulate the production of outer membrane vesicles and tubes by Francisella. *Mol.*
630 *Microbiol.* 107(4):523-541.

631 20. Chong GW, Pirbadian S, & El-Naggar MY (2019) Surface-Induced Formation and Redox-
632 Dependent Staining of Outer Membrane Extensions in Shewanella oneidensis MR-1. *Front.*
633 *Energy Res.* 7.
634 21. Subramanian P, Pirbadian S, El-Naggar MY, & Jensen GJ (2018) Ultrastructure of Shewanella
635 oneidensis MR-1 nanowires revealed by electron cryotomography. *Proc. Natl. Acad. Sci. U. S. A.*
636 115(14):E3246-E3255.
637 22. Pirbadian S*, et al.* (2014) Shewanella oneidensis MR-1 nanowires are outer membrane and
638 periplasmic extensions of the extracellular electron transport components. *Proc. Natl. Acad. Sci.*
639 *U. S. A.* 111(35):12883-12888.
640 23. Gorby YA*, et al.* (2006) Electrically conductive bacterial nanowires produced by Shewanella
641 oneidensis strain MR-1 and other microorganisms. *Proc. Natl. Acad. Sci. U. S. A.* 103(30):11358-
642 11363.
643 24. Bhattacharya S*, et al.* (2019) A Ubiquitous Platform for Bacterial Nanotube Biogenesis. *Cell Rep*.
644 25. Dubey GP*, et al.* (2016) Architecture and Characteristics of Bacterial Nanotubes. *Dev. Cell*
645 36(4):453-461.
646 26. Dubey GP & Ben-Yehuda S (2011) Intercellular nanotubes mediate bacterial communication. *Cell*
647 144(4):590-600.
648 27. Pande S*, et al.* (2015) Metabolic cross-feeding via intercellular nanotubes among bacteria. *Nat*
649 *Commun* 6:6238.
650 28. Tanaka M, Arakaki A, & Matsunaga T (2010) Identification and functional characterization of
651 liposome tubulation protein from magnetotactic bacteria. *Mol. Microbiol.* 76(2):480-488.
652 29. Danne L*, et al.* (2017) Membrane Remodeling by a Bacterial Phospholipid-Methylating Enzyme.
653 *MBio* 8(1).
654 30. Danne L*, et al.* (2017) Dissection of membrane-binding and -remodeling regions in two classes of
655 bacterial phospholipid N-methyltransferases. *Biochim. Biophys. Acta* 1859(12):2279-2288.
656 31. Danne L*, et al.* (2015) Membrane-binding mechanism of a bacterial phospholipid N-
657 methyltransferase. *Mol. Microbiol.* 95(2):313-331.
658 32. Low HH, Sachse C, Amos LA, & Lowe J (2009) Structure of a bacterial dynamin-like protein lipid
659 tube provides a mechanism for assembly and membrane curving. *Cell* 139(7):1342-1352.
660 33. Low HH & Lowe J (2006) A bacterial dynamin-like protein. *Nature* 444(7120):766-769.
661 34. Bohuszewicz O, Liu J, & Low HH (2016) Membrane remodelling in bacteria. *J. Struct. Biol.*
662 196(1):3-14.
663 35. Nealson KH & Scott J (2006) Ecophysiology of the Genus Shewanella.1133-1151.
664 36. Marsili E*, et al.* (2008) Shewanella secretes flavins that mediate extracellular electron transfer.
665 *Proceedings of the National Academy of Sciences* 105(10):3968-3973.
666 37. Gorby Y*, et al.* (2008) Redox-reactive membrane vesicles produced by Shewanella. *Geobiology*
667 6(3):232-241.
668 38. Liu X*, et al.* (2019) Bacterial Vesicles Mediate Extracellular Electron Transfer. *Environmental*
669 *Science & Technology Letters*.
670 39. Xu S, Barrozo A, Tender LM, Krylov AI, & El-Naggar MY (2018) Multiheme Cytochrome Mediated
671 Redox Conduction through Shewanella oneidensis MR-1 Cells. *J. Am. Chem. Soc.* 140(32):10085-
672 10089.
673 40. Okamoto A, Nakamura R, & Hashimoto K (2011) In-vivo identification of direct electron transfer
674 from Shewanella oneidensis MR-1 to electrodes via outer-membrane OmcA–MtrCAB protein
675 complexes. *Electrochim. Acta* 56(16):5526-5531.
676 41. Cox J*, et al.* (2014) Accurate proteome-wide label-free quantification by delayed normalization
677 and maximal peptide ratio extraction, termed MaxLFQ. *Mol. Cell. Proteomics* 13(9):2513-2526.

678 42. Hsu VW, Bai M, & Li J (2012) Getting active: protein sorting in endocytic recycling. *Nat. Rev. Mol.*
679 *Cell Biol.* 13(5):323-328.
680 43. Vincent TL, Green PJ, & Woolfson DN (2013) LOGICOIL--multi-state prediction of coiled-coil
681 oligomeric state. *Bioinformatics* 29(1):69-76.
682 44. Linkner J*, et al.* (2014) The inverse BAR domain protein IBARa drives membrane remodeling to
683 control osmoregulation, phagocytosis and cytokinesis. *J. Cell Sci.* 127(Pt 6):1279-1292.
684 45. Cui H*, et al.* (2013) Understanding the role of amphipathic helices in N-BAR domain driven
685 membrane remodeling. *Biophys. J.* 104(2):404-411.
686 46. Henne WM*, et al.* (2007) Structure and analysis of FCHo2 F-BAR domain: a dimerizing and
687 membrane recruitment module that effects membrane curvature. *Structure* 15(7):839-852.
688 47. Roy A, Kucukural A, & Zhang Y (2010) I-TASSER: a unified platform for automated protein
689 structure and function prediction. *Nat. Protoc.* 5(4):725-738.
690 48. Moravcevic K*, et al.* (2015) Comparison of Saccharomyces cerevisiae F-BAR domain structures
691 reveals a conserved inositol phosphate binding site. *Structure* 23(2):352-363.
692 49. van Weering JR & Cullen PJ (2014) Membrane-associated cargo recycling by tubule-based
693 endosomal sorting. *Semin. Cell Dev. Biol.* 31:40-47.
694 50. Pylypenko O, Lundmark R, Rasmuson E, Carlsson SR, & Rak A (2007) The PX-BAR membrane-
695 remodeling unit of sorting nexin 9. *EMBO J.* 26(22):4788-4800.
696 51. Vinogradov E, Korenevsky A, & Beveridge TJ (2003) The structure of the rough-type
697 lipopolysaccharide from Shewanella oneidensis MR-1, containing 8-amino-8-deoxy-Kdo and an
698 open-chain form of 2-acetamido-2-deoxy-d-galactose. *Carbohydr. Res.* 338(19):1991-1997.
699 52. Daumke O, Roux A, & Haucke V (2014) BAR domain scaffolds in dynamin-mediated membrane
700 fission. *Cell* 156(5):882-892.
701 53. Schoneberg J*, et al.* (2017) Lipid-mediated PX-BAR domain recruitment couples local membrane
702 constriction to endocytic vesicle fission. *Nat Commun* 8:15873.
703 54. Pinheiro PS*, et al.* (2014) The BAR domain protein PICK1 controls vesicle number and size in
704 adrenal chromaffin cells. *J. Neurosci.* 34(32):10688-10700.
705 55. Meyer AJ, Segall-Shapiro TH, Glassey E, Zhang J, & Voigt CA (2018) Escherichia coli "Marionette"
706 strains with 12 highly optimized small-molecule sensors. *Nat. Chem. Biol.*
707 56. Mahmood MI, Noguchi H, & Okazaki KI (2019) Curvature induction and sensing of the F-BAR
708 protein Pacsin1 on lipid membranes via molecular dynamics simulations. *Sci. Rep.* 9(1):14557.
709 57. Wang Q*, et al.* (2009) Molecular mechanism of membrane constriction and tubulation mediated
710 by the F-BAR protein Pacsin/Syndapin. *Proc. Natl. Acad. Sci. U. S. A.* 106(31):12700-12705.
711 58. Bird LJ*, et al.* (2018) Development of a Genetic System for Marinobacter atlanticus CP1 (sp.
712 nov.), a Wax Ester Producing Strain Isolated From an Autotrophic Biocathode. *Front. Microbiol.*
713 9:3176.
714 59. Coursolle D & Gralnick JA (2010) Modularity of the Mtr respiratory pathway of Shewanella
715 oneidensis strain MR-1. *Mol. Microbiol.* 77(4):995-1008.
716 60. Bird LJ*, et al.* (2019) Engineered living conductive biofilms as functional materials. *MRS*
717 *Commun.*:1-13.
718 61. Ayton GS*, et al.* (2009) New insights into BAR domain-induced membrane remodeling. *Biophys.*
719 *J.* 97(6):1616-1625.
720 62. Simunovic M*, et al.* (2013) Protein-mediated transformation of lipid vesicles into tubular
721 networks. *Biophys. J.* 105(3):711-719.
722 63. Noguchi H (2016) Membrane tubule formation by banana-shaped proteins with or without
723 transient network structure. *Sci. Rep.* 6:20935.
724 64. Stachowiak JC*, et al.* (2012) Membrane bending by protein-protein crowding. *Nat. Cell Biol.*
725 14(9):944-949.

726 65. Frohlich C*, et al.* (2013) Structural insights into oligomerization and mitochondrial remodelling of
727 dynamin 1-like protein. *EMBO J.* 32(9):1280-1292.
728 66. Ford MG*, et al.* (2002) Curvature of clathrin-coated pits driven by epsin. *Nature* 419(6905):361-
729 366.
730 67. Yoon Y*, et al.* (2010) Molecular basis of the potent membrane-remodeling activity of the epsin 1
731 N-terminal homology domain. *J. Biol. Chem.* 285(1):531-540.
732 68. Salzer U, Kostan J, & Djinovic-Carugo K (2017) Deciphering the BAR code of membrane
733 modulators. *Cell. Mol. Life Sci.* 74(13):2413-2438.
734 69. Perez-Cruz C*, et al.* (2013) New type of outer membrane vesicle produced by the Gram-negative
735 bacterium Shewanella vesiculosa M7T: implications for DNA content. *Appl. Environ. Microbiol.*
736 79(6):1874-1881.
737 70. Hagen WJH, Wan W, & Briggs JAG (2017) Implementation of a cryo-electron tomography tilt-
738 scheme optimized for high resolution subtomogram averaging. *J. Struct. Biol.* 197(2):191-198.
739 71. Rohou A & Grigorieff N (2015) CTFFIND4: Fast and accurate defocus estimation from electron
740 micrographs. *J. Struct. Biol.* 192(2):216-221.
741 72. Kremer JR, Mastronarde DN, & McIntosh JR (1996) Computer visualization of three-dimensional
742 image data using IMOD. *J. Struct. Biol.* 116(1):71-76.
743 73. Brown RN, Romine MF, Schepmoes AA, Smith RD, & Lipton MS (2010) Mapping the subcellular
744 proteome of Shewanella oneidensis MR-1 using sarkosyl-based fractionation and LC-MS/MS
745 protein identification. *J. Proteome Res.* 9(9):4454-4463.
746 74. Nielsen H (2017) Predicting Secretory Proteins with SignalP. *Protein Function Prediction:*
747 *Methods and Protocols*, ed Kihara D (Springer New York, New York, NY), pp 59-73.
748 75. Altschul SF*, et al.* (1997) Gapped BLAST and PSI-BLAST: a new generation of protein database
749 search programs. *Nucleic Acids Res.* 25(17):3389-3402.
750 76. Finn RD, Clements J, & Eddy SR (2011) HMMER web server: interactive sequence similarity
751 searching. *Nucleic Acids Res.* 39(Web Server issue):W29-37.
752 77. Le SQ & Gascuel O (2008) An improved general amino acid replacement matrix. *Mol. Biol. Evol.*
753 25(7):1307-1320.
754 78. Freeman GH & Halton JH (1951) Note on an exact treatment of contingency, goodness of fit and
755 other problems of significance. *Biometrika* 38(1-2):141-149.
756 79. Myers CR & Nealson KH (1988) Bacterial manganese reduction and growth with manganese
757 oxide as the sole electron acceptor. *Science* 240(4857):1319-1321.
758 80. Saltikov CW & Newman DK (2003) Genetic identification of a respiratory arsenate reductase.
759 *Proc. Natl. Acad. Sci. U. S. A.* 100(19):10983-10988.
760 81. Kovach ME*, et al.* (1995) Four new derivatives of the broad-host-range cloning vector
761 pBBR1MCS, carrying different antibiotic-resistance cassettes. *Gene* 166(1):175-176.
762 82. Simon R, Priefer U, & Pühler A (1983) A Broad Host Range Mobilization System for In Vivo
763 Genetic Engineering: Transposon Mutagenesis in Gram Negative Bacteria. *Biotechnology. (N. Y.)*
764 1(9):784-791.

765

766

767

768

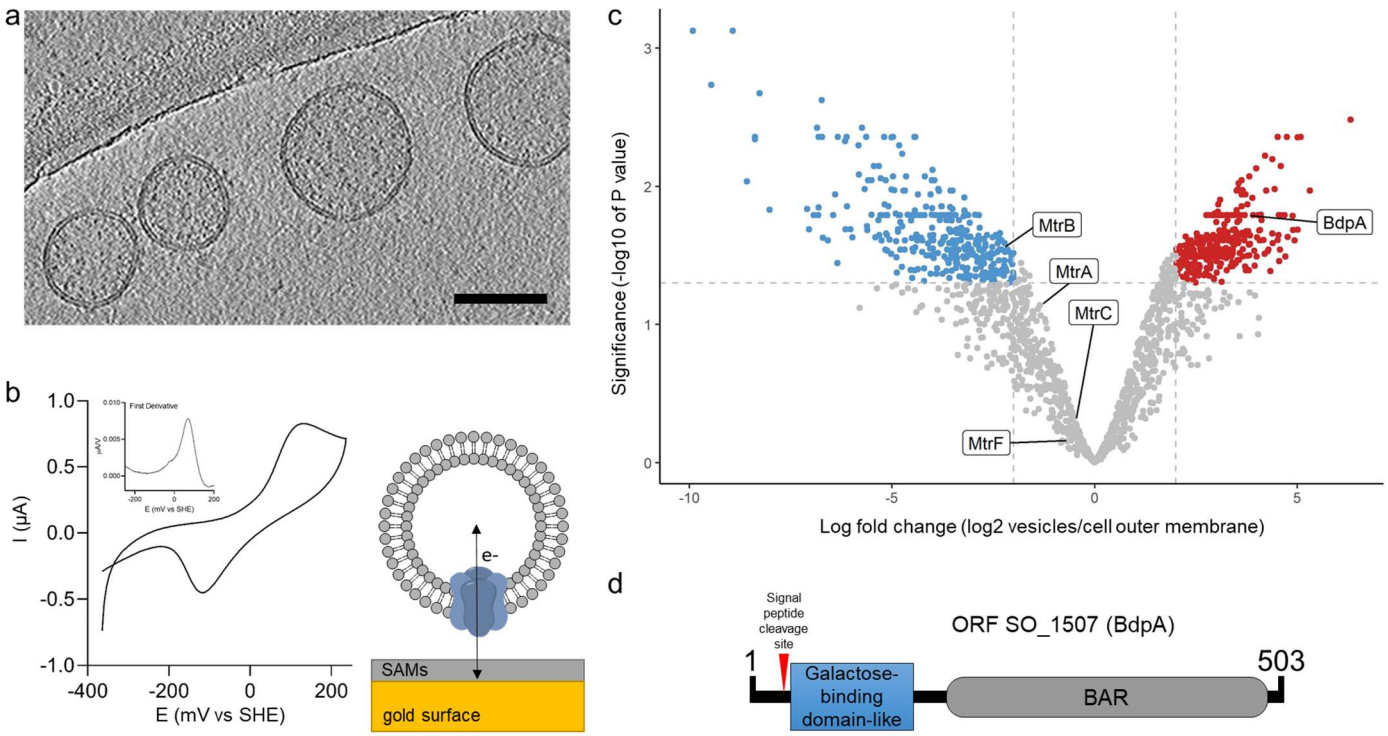

Fig. 1| Redox active vesicles are enriched with BAR domain protein BdpA. a. Cryoelectron tomography image of *S. oneidensis* MR-1 outer membrane vesicles (OMVs) (scale = 200 nm). **b**. Cyclic voltammetry of vesicles adhered to gold electrode via small self-assembled monolayers, as diagramed. Inset shows first derivative of anodic scan. **c**. Volcano plot of vesicle proteome compared to cell-associated outer membrane (red = enriched in vesicles, blue = enriched in cell-associated outer membrane). **d**. Schematic of BdpA domains.

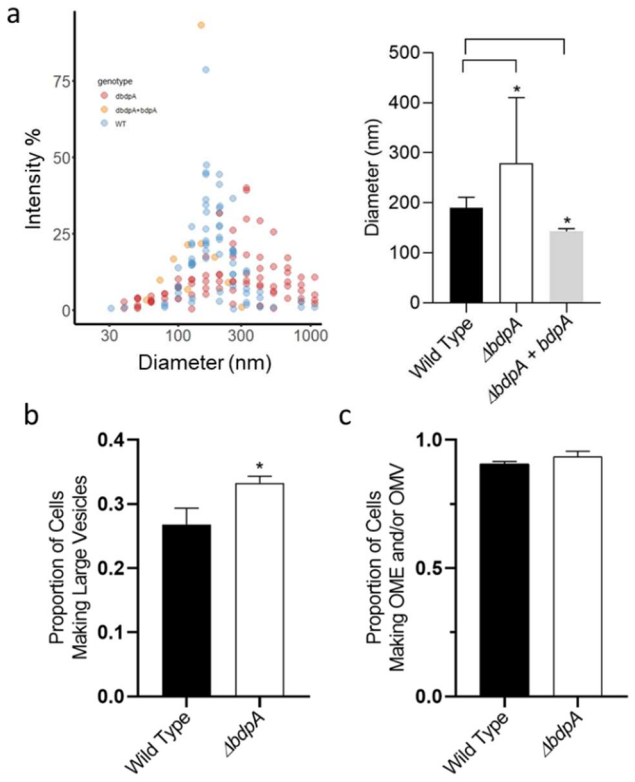

Fig. 2| BdpA is responsible for maintaining vesicle size but does not alter the frequency of OMV or OME formation. a. Dynamic light scattering of OMV size distributions from the deletion strain (red, 9 biological replicates) compared to wild type (blue, 11 biological replicates) and Δ*bdpA* cells expressing *bdpA* from a plasmid (yellow, (left), with weighted averages of OMV diameters (right). Color opacity denotes overlapping data points ($p < 0.05$, *t*-test). **b**. Proportion of cells forming large vesicles (>300 nm diameter) during perfusion flow monitored by time lapse fluorescence imaging ($p < 0.00459$, χ^2 test). **c**. Proportion of cells forming vesicles and extensions relative to the total number of cells observed by fluorescence microscopy during perfusion flow ($p > 0.05$, χ^2 test). Time lapse images were recorded from 3 biological replicates per strain with 5-13 fields of view per replicate. Error bars represent standard deviation.

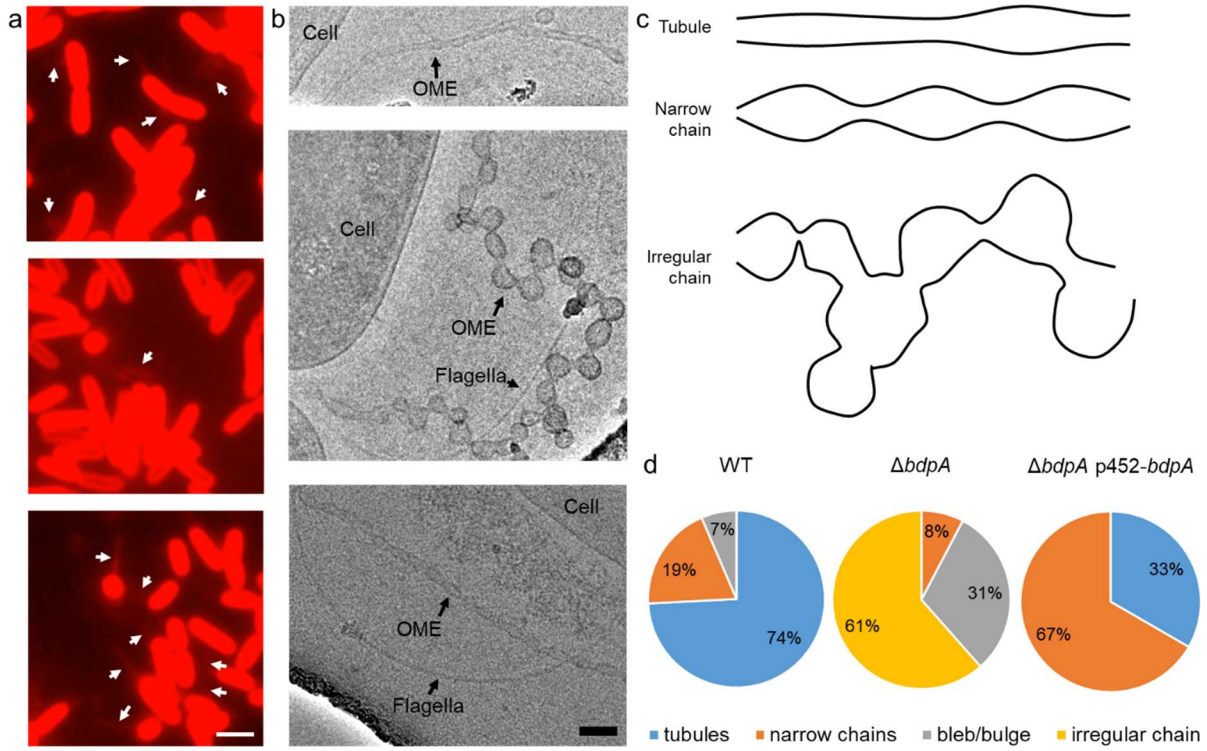

Fig. 3| BdpA promotes OME maturation into ordered tubules. a. Fluorescence images of *S. oneidensis* WT (top), Δ*bdpA* (middle), and Δ*bdpA* p452-*bdpA* with 12.5 μM DAPG (bottom) OMEs. Scale = 2 μm. **b.** Cryo-TEM images of WT (top), Δ*bdpA* (middle), and Δ*bdpA* p452-*bdpA* with 12.5 μM DAPG (bottom) OMEs. Scale = 100 nm. **c.** Representative cartoon of OME phenotypes. **d**. Pie charts show relative frequency of OME phenotypes observed from each strain. Membrane blebs/bulges were defined as non-structured membrane protrusions that did not resemble either of the other OME categories.

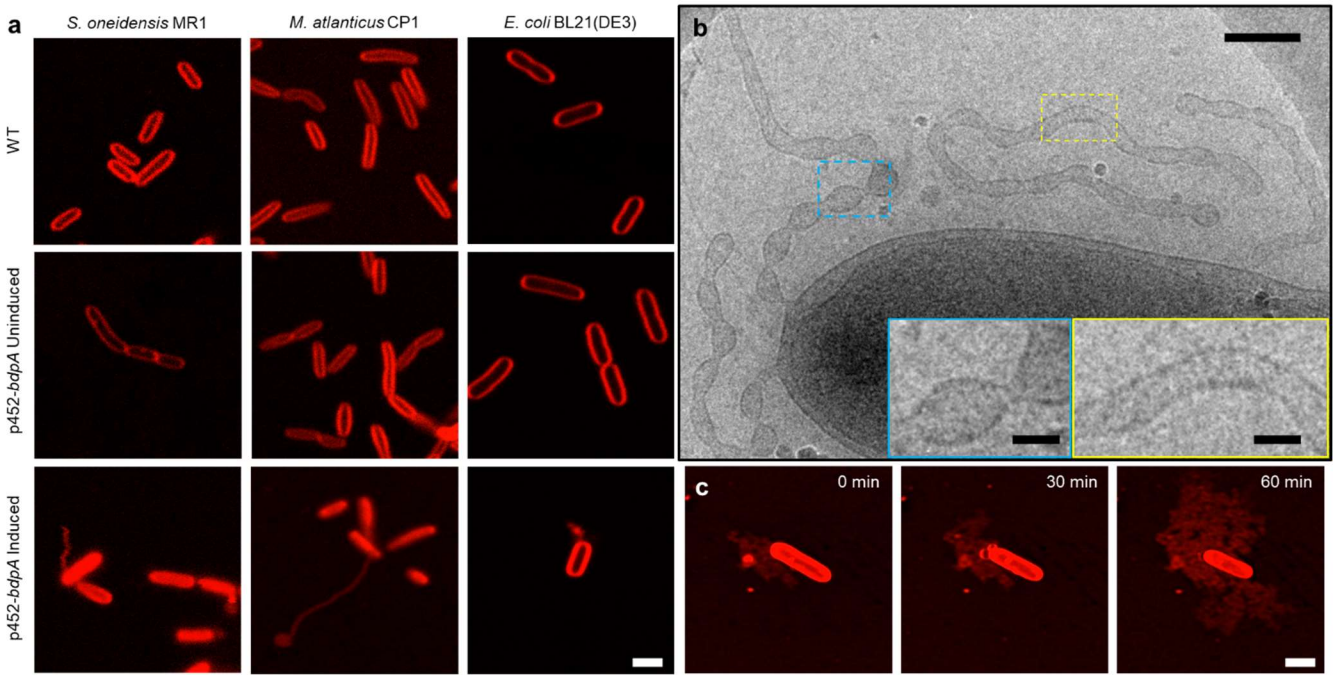

Fig. 4| Heterologous expression of BdpA promotes OME formation. a. Induction of BdpA expression with 12.5 μM DAPG during planktonic, non-attached growth results in OME formation in *S. oneidensis* (left), *M. atlanticus* CP1 (middle), and *E. coli* BL21(DE3) (right). Scale = 2 μm. **b.** Cryo-TEM image of OMEs following planktonic induction of BdpA expression in *S. oneidensis* WT p452-*bdpA* cells. Scale = 200 nm. Insets enlarged to show detail of regularly ordered electron densities at the surface of OME junctions (blue) and tubule regions (yellow). Scale = 50 nm. **c.** OME growth over time at 30 minute intervals of *E. coli* BL21(DE3) expressing BdpA while attached to a glass surface. Scale = 2 μm.

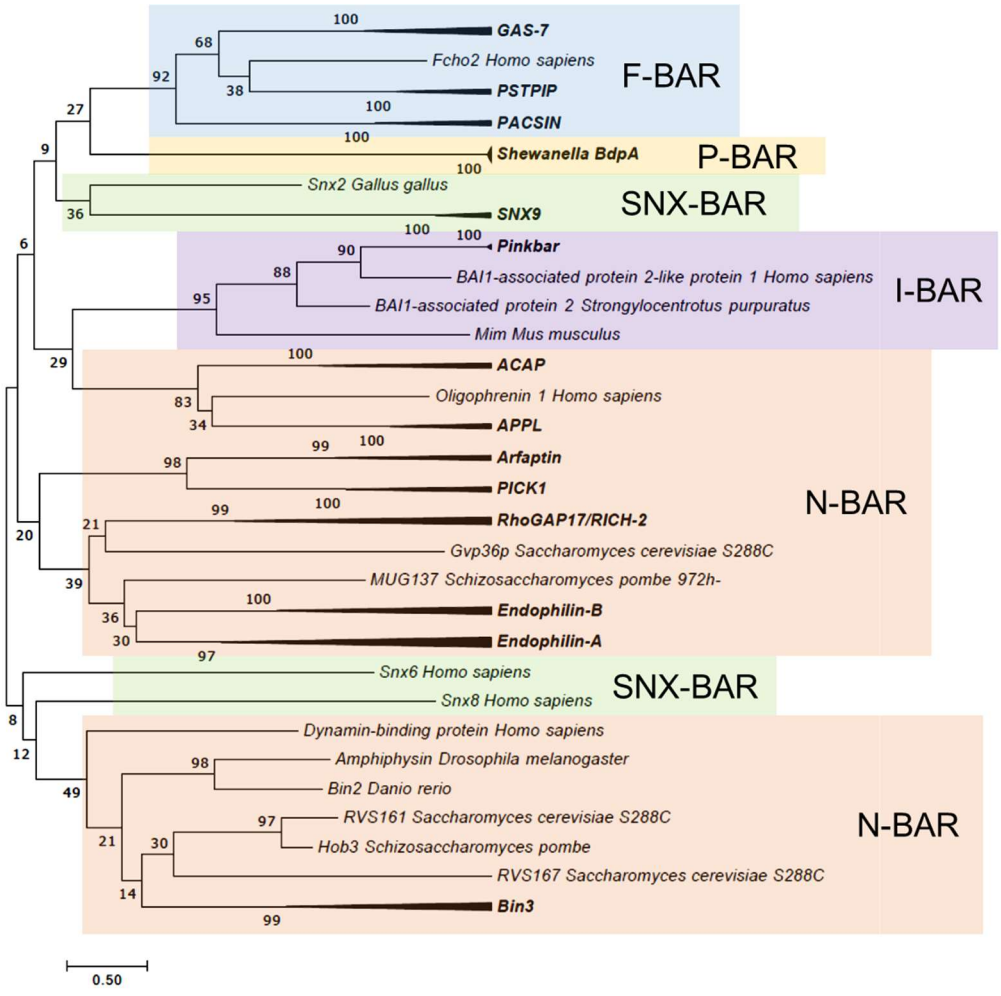

Fig. 5| Comparative phylogenetic analysis of BdpA with prokaryotic homologs and eukaryotic BAR domains. Maximum Likelihood evolutionary histories were inferred from 1000 bootstrap replicates, and the percentage of trees in which the taxa clustered together is shown next to the branches. Arrows indicate multiple branches collapsed to a single node. *S. oneidensis* BdpA and 5 prokaryotic orthologs (WP_011623497 – unclassified *Shewanella*, ESE40074 – *S. decolorationis* S12, WP_039978560 - *S. decolorationis*, KEK29176 – *S. xiamenensis*, and WP_055648003 – *Shewanella sp.* Sh95) predicted by the current BAR domain Pfam HMM to contain a BAR domain aligned with representative BAR domains from various BAR domain subtypes (N-BAR, F-BAR, SNX-BAR, I-BAR) at a total of 196 positions. The Gamma distribution used to model evolutionary rate differences among sites was 12.9598.

828 **Supplemental Table 2**

829

830

Strain, Plasmid, or Primer	Description or relevant genotype	Source or reference
Strains		
Shewanella oneidensis strains		
MR-1	Wild type	[(79)]
Δ*bdpA*	*bdpA* scarless deletion	This study
Marinobacter atlanticus CP1	Wild type	[(58)]
Eschericia coli strains		
BL21(DE3)	OneShot *E. coli* BL21(DE3)	Invitrogen
UQ950	Cloning strain	[(80)]
BW29427 (WM3064)	Conjugation strain	[(80)]
Plasmids		
pBBR1-mcs2	empty vector	[(81)]
pBBJM	Cloning backbone	This study
pSMV3	Suicide vector	[(82)]
pSMV3_1507KO	Contains up and downstream regions of SO_1507	This study
p452-*bdpA*	DAPG inducible *bdpA* vector	This study
Primers		
pAJMF2	TTAACGCGAATTTTAACAAAATATTAACGCcccgcttaacgatcgttggctg	
pAJMR3	AGCGGATAACAATTTCACACAGGAAACAGCTacctcagataaaatatttgc	
pBBRF3	gggctcatgagcaaatattttatctgaggtAGCTGTTTCCTGTGTGAAATTG	
pBBRR2	acccgcgctcagccaacgatcgttaagcgggGCGTTAATATTTTGTTAAAATTCGC	
1507F_insert	ttaatactagagaaagaggggaaatactagATGCGCACCGCTGC	
1507R_insert	gaggcctcttttctggaatttggtaccgagCTACATAAAGGCTTTAGTAAAGGCTT	
BBJMV_reverse	CAGCATTGAGATGACTGCAGCGGTGCGCATctagtatttcccctctttctctagtat	
BBJMV_forward	AAGGAAGCCTTTACTAAAGCCTTTATGTAGctcggtaccaaattccagaaaag	

831

832

833 **Supplemental Figure 1**

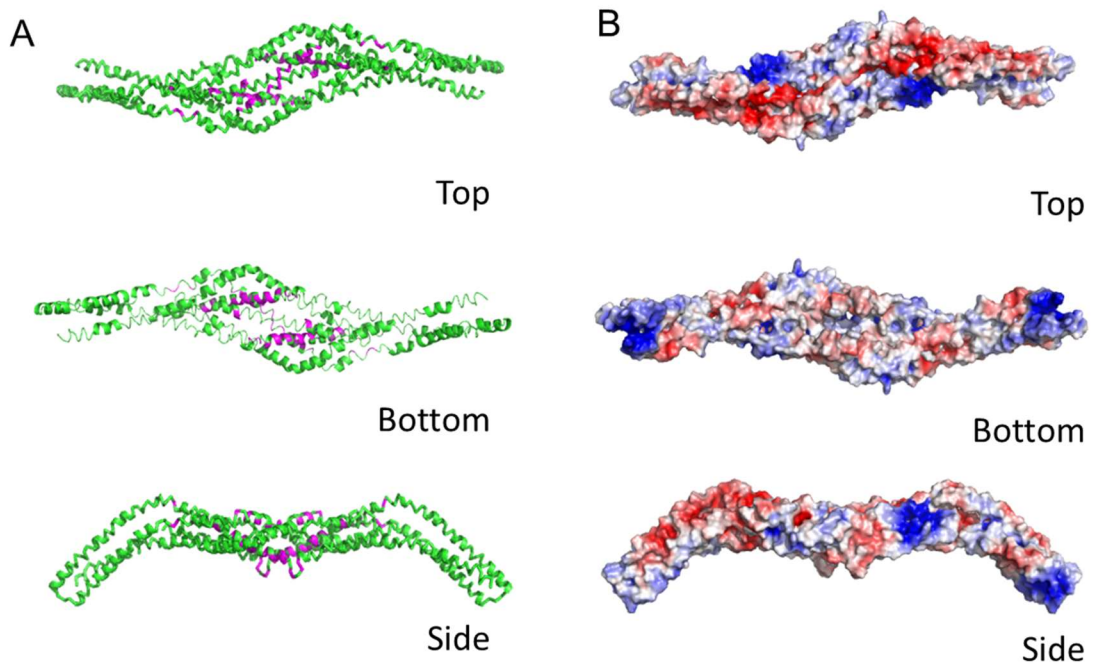

834

835 **Predicted structure of the BAR domain region of BdpA.**
(A) Ribbon diagram of i-TASSER prediction of BdpA structure as a dimeric molecule, residues 175-502. Dimer was modeled from an alignment of BdpA monomers to homodimeric Hof1p (Protein Data Bank [PDB] ID code 4WPE) structures that resulted in closest proximity of putative dimer interface (purple) residues from the initial BAR domain prediction. (B) Surface representation of predicted BdpA homodimer colored according to electrostatic potential. The bottom concave face has an accumulation of distributed positively charged residues (Lys, Arg, His - blue), while the top face has clusters of positive and negatively charged (Glu, Asp - red) residues, within a range of -3.0 to 3.0 V.

836 **Supplemental Figure 2**

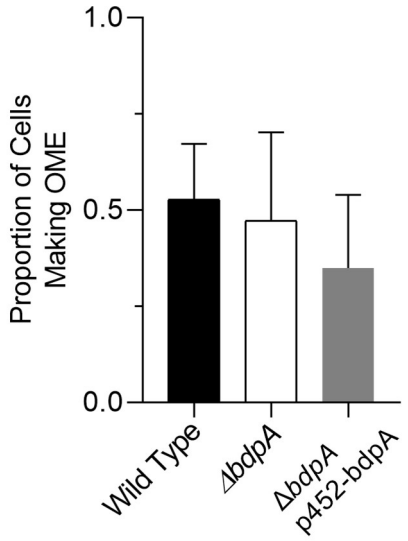

837

838 Proportion of cells making OMEs without perfusion flow at three hours post deposition onto
839 chambered cover glass, measured from five random fields of view from each of three
840 independent cultures per strain.

841

842 **Supplemental Figure 3**

843

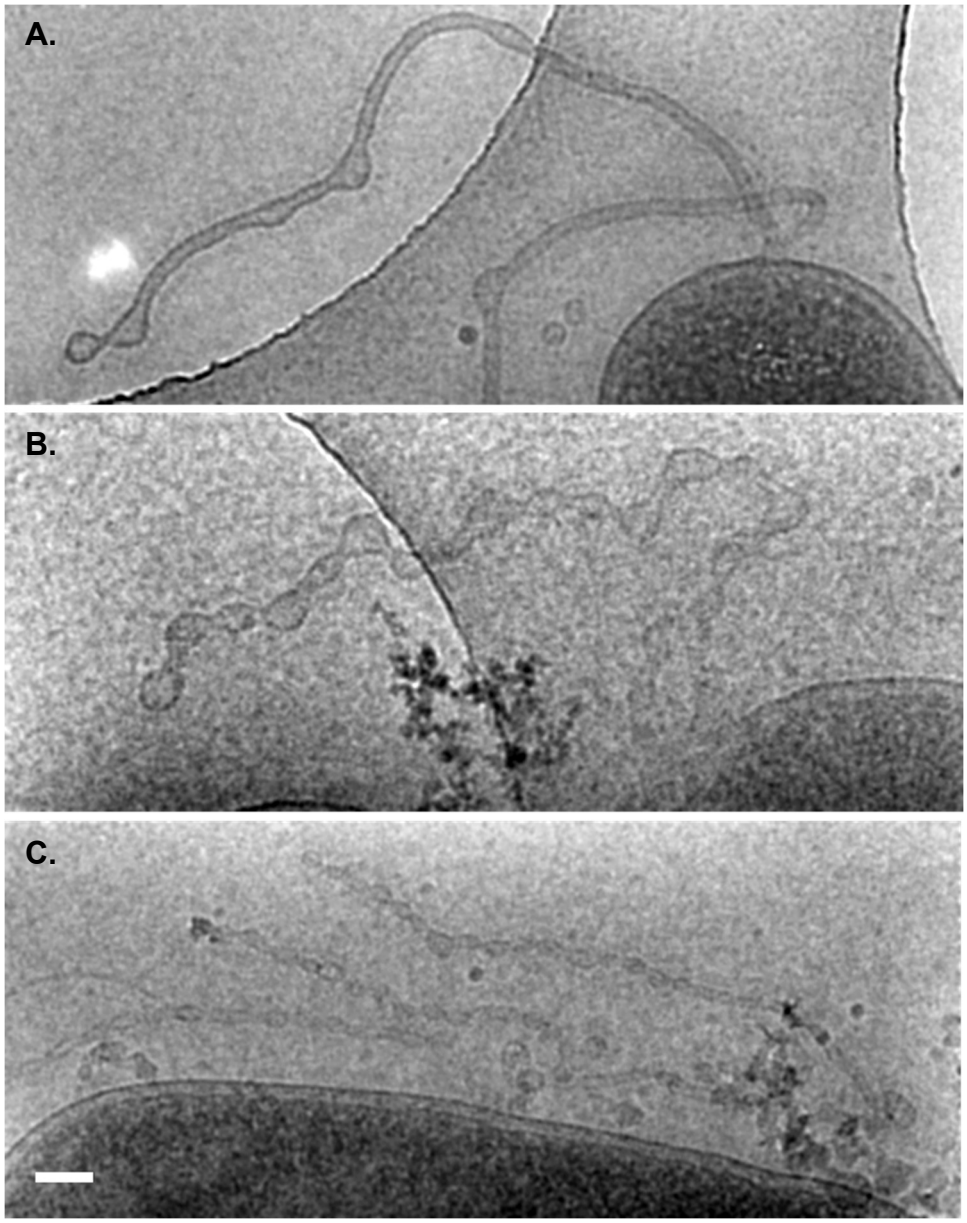

844

845 Cryo-TEM of *S. oneidensis* WT (A), Δ*bdpA* (B), and Δ*bdpA* p452-*bdpA* (C) OMEs at 90
846 minutes post-surface attachment. Scale = 100 nm.

847

848 **Supplemental Figure 4**

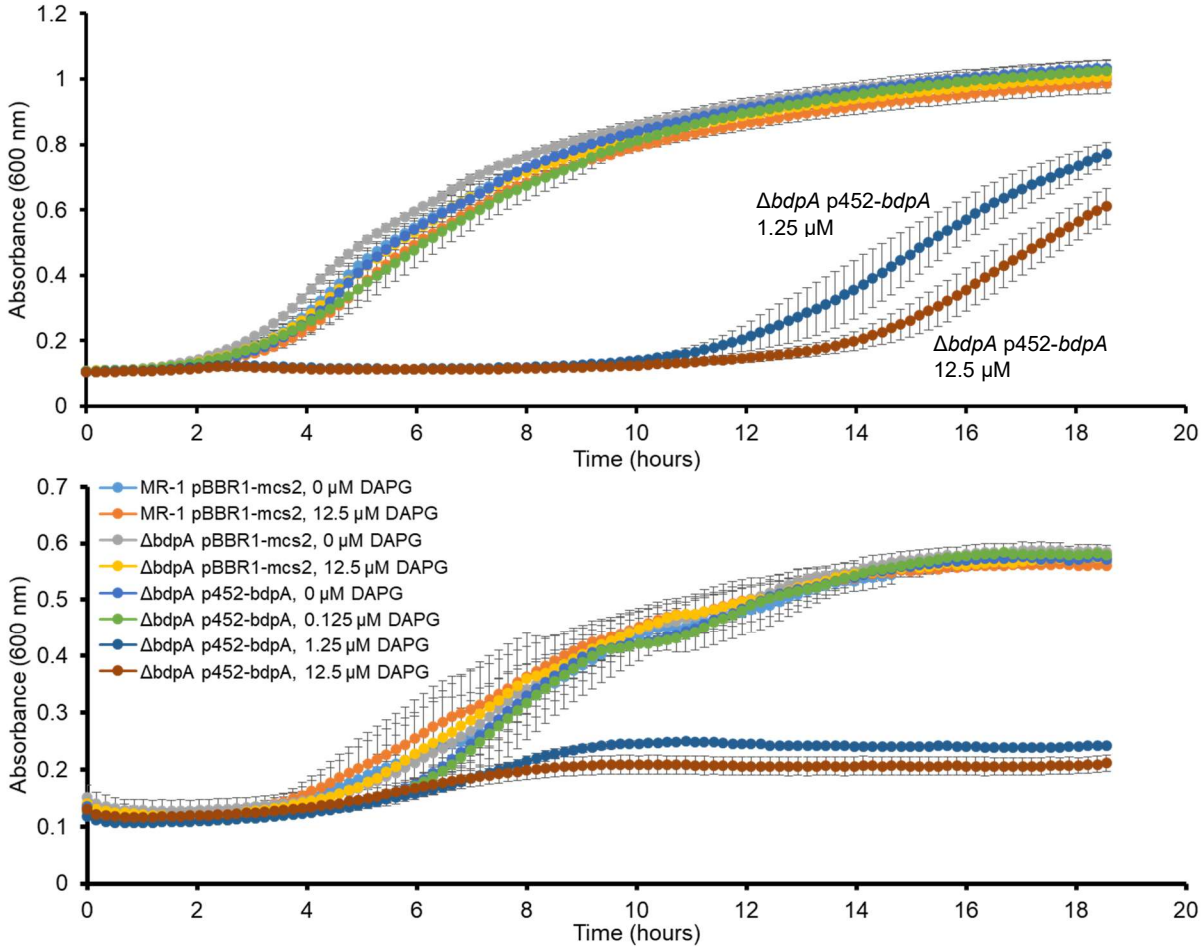

849

850 Growth of *S. oneidensis* strains in LB (top) or *Shewanella* Defined Medium (SDM)
851 (bottom) in response to DAPG exposure and BdpA induction. Error bars are standard
852 deviation of three biological replicates.

853

854 **Supplemental Figure 5**

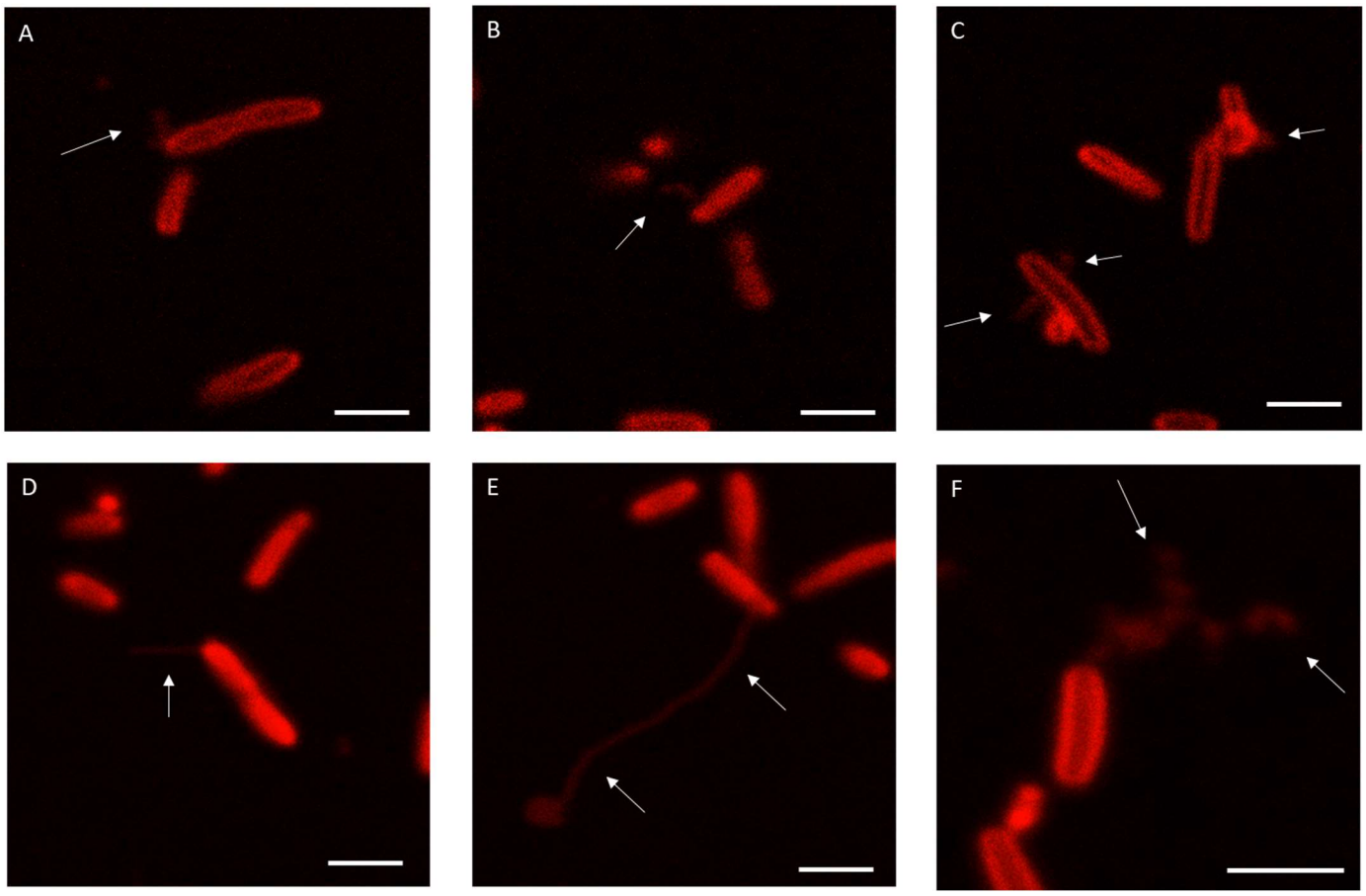

855

856 **Variability in OME phenotypes following BdpA induction in *M. atlanticus* CP1**
857 **p452-*bdpA* cells.** Cells displayed an array of membrane curvature phenotypes, ranging
858 from short OMEs (<2µm, A-C), long OMEs (2-10+ µm, D-F), membrane blebbing (C,F),
859 and branched OME/OMV chains (F). Scale = 2 µm.

860

861 **Supplemental Figure 6**

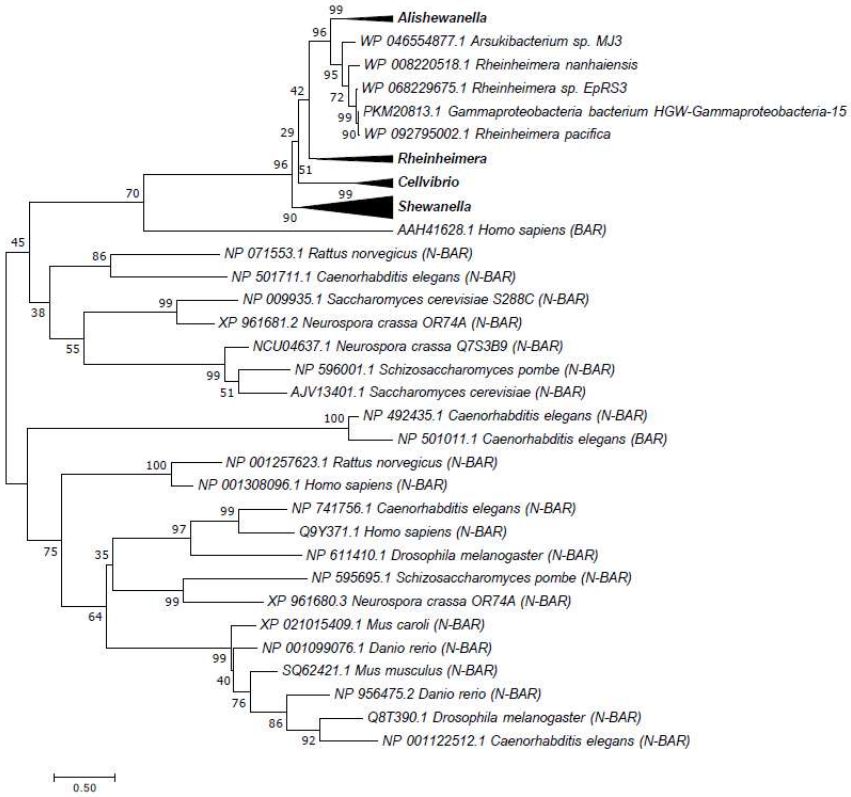

862

863 **BdpA has homologs in other bacterial species.** A phylogenetic tree of the 23 BAR
864 domain sequences that seed the BAR domain HMM predictions, *S. oneidensis* BdpA,
865 and conserved BdpA orthologs in other prokaryotes. The protein regions corresponding
866 to the BdpA BAR domain sequence from the 52 prokaryotic BdpA orthologs were
867 aligned with the 23 representative eukaryotic BAR domain-containing proteins used to
868 generate the BAR domain consensus sequence (cd07307) at a total of 222 positions.
869 Maximum Likelihood evolutionary histories were inferred from 1000 bootstrap replicates,
870 and the percentage of trees in which the taxa clustered together is shown next to the
871 branches. The Gamma distribution used to model evolutionary rate differences among
872 sites was 11.9548.

873

874 **Supplementary Video 1** Widefield imaging of *S. oneidensis* WT cells 3h post-
875 deposition onto the surface of a chambered cover glass. Scale = 5 μm.

876

877 **Supplementary Video 2** Widefield imaging of *S. oneidensis* Δ*bdpA* cells 3h post-
878 deposition onto the surface of a chambered cover glass. Scale = 5 μm.

879

880 **Supplementary Video 3** Widefield imaging of *S. oneidensis* Δ*bdpA* p452-*bdpA* cells 3h
881 post-deposition onto the surface of a chambered cover glass. Scale = 5 μm.

882

883 **Supplementary Video 4** Confocal imaging of *S. oneidensis* MR-1 p452-*bdpA* cells after
884 1h planktonic induction of BdpA with 12.5 μM DAPG. Scale = 5 μm.

885